Nano Energy 89 (2021) 106452

Contents lists available at ScienceDirect

Nano Energy

journal homepage: www.elsevier.com/locate/nanoen

Interfaces-dominated Li_2S nucleation behavior enabled by heterostructure catalyst for fast kinetics Li-S batteries

Da-Qian Cai [a,b], Jin-Lin Yang [a], Ting Liu [c], Shi-Xi Zhao [a,*], Guozhong Cao [d,*]

[a] Tsinghua Shenzhen International Graduate School, Tsinghua University, Shenzhen 518055, China
[b] School of Materials Science and Engineering, Tsinghua University, Beijing 100084, China
[c] Foshan (Southern China) Institute for New Materials, Foshan 528200, China
[d] Department of Materials Science and Engineering, University of Washington, Seattle, WA 98195, USA

ARTICLE INFO

Keywords:
Lithium-sulfur batteries
MoO_2/α-MoC
Cathode additives
Catalytic effect
Li_2S deposition

ABSTRACT

Lithium-sulfur batteries (LSBs) have gained wide attention in the past decades for its high energy density and low cost. However, LSBs practical application is hindered by the severe shuttling of soluble intermediate lithium polysulfides (LiPSs), and the uncontrollable deposition of insulating Li_2S, which limits the active species utilization and decelerates the redox kinetics. In this study, MoO_2/α-MoC nanocomposite was investigated as a multifunctional electrocatalyst to address above problems. Not only does such electrocatalyst immobilizes LiPSs on its surface but also facilitate the subsequent conversion reaction, further enable the heterogeneous Li_2S nucleation and induce three-dimensional precipitation of Li_2S. MoO_2/α-MoC-containing LSBs exhibit excellent rate performance, promising cycling stability, and a high specific capacity of 1177 mAh g^{-1} at 0.2 C and 695 mAh g^{-1} at 3 C with a low-capacity deterioration. Good cyclic stability was achieved at 0.5 C even with a high sulfur loading of 5 mg cm^{-2} and a low E/S ratio of 6–7 μL mg^{-1} by employing a MoO_2/α-MoC interlayer.

1. Introduction

Lithium-sulfur batteries (LSBs) has been considered as one of the promising next-generation energy storage systems due to its high theoretical specific capacity (1675 mAh g^{-1}), high energy density (2600 Wh kg^{-1}), non-toxicity and abundant sulfur reserves [1,2]. However, the large-scale commercialization of LSBs is hindered by several key obstacles: (1) the electronic insulation nature of sulfur and its discharge products (10^{-30} S cm^{-1} for S_8 and 10^{-17} S cm^{-1} for Li_2S); (2) sluggish redox conversion kinetics and severe "shuttle effect" of soluble intermediate lithium polysulfides (Li_2S_x, $4 \leq x \leq 8$), and (3) huge volume fluctuation during charge/discharge process [3,4]. Above problems will lead to insufficient utilization of sulfur, low discharge capacity, self-discharge, fast capacity decay, low energy efficiency and low power density.

In the past decades, numerous efforts have been made to address the above obstacles, such as designing appropriate sulfur host materials to physically confine and/or chemically anchor sulfur species. Typically, nanostructured carbonaceous materials are employed as sulfur hosts to circumvent the issues of poor conductivity [5–7]. The abundant pores and large specific surface area of the carbon skeleton provide sufficient spaces for sulfur loading, buffering volume expansion and physically confining sulfur species. However, carbon materials can only physically adsorb lithium polysulfides (LiPSs) through weak van der Waals force, which is inadequate to inhibit its shuttling. It has been demonstrated that employing materials with high polarity and electronegativity (i.e. oxides, sulfides, nitrides, carbides, phosphates, borides, MXene, etc.) as sulfur hosts or functional interlayers can effectively chemisorb LiPSs and thereby inhibit its shuttling [8–13]. The adsorbed intermediate LiPSs will accumulate on the cathode surface, resulting in limited conversion efficiency and shuttling of LiPSs driven by the concentration gradient [14]. In brief, the poor conductivity makes the discharge products Li_2S difficult to activate, and the dissolution of the intermediate products in the electrolyte increases the electrolyte concentration and thus hinders Li^+ ion migrations. The volumetric expansion leads to the active material peeling from the collector and the inability to capture electrons efficiently are other remaining challenges. Confining the active materials and simultaneously providing mild adsorption and rapid transport are considered to be an effective means to tackle the multiple obstacles. Introducing appropriate catalysts for realizing the solid-liquid-solid conversion of sulfur species has been recognized necessary to attain desired LSBs performance [15,16].

* Corresponding authors.
E-mail addresses: zhaosx@sz.tsinghua.edu.cn (S.-X. Zhao), gzcao@uw.edu (G. Cao).

https://doi.org/10.1016/j.nanoen.2021.106452
Received 30 June 2021; Received in revised form 9 August 2021; Accepted 17 August 2021
Available online 20 August 2021

The surface defects of polar materials such as edges or dangling bonds are capable of providing catalytic sites for trapping LiPSs and promoting its conversion [9,17]. Recently, two-in-one heterostructure catalysts has been demonstrated to synergistically integrate the merits of each component in one catalysts [18–20]. Heterostructure mediators (i.e., TiO_2-TiN [21], MoO_2-Mo_2N [22], Fe_2O_3-Fe_3C [23], V_2O_3/V_8C_7 [24], MoC@MoO_x [25], TiO_2–Ni_3S_2 [26] etc.) constructed with high polarity, better conductivity and redox catalytic activity nanocrystals hybrids have been exploited to improve the performance of LSBs. The binary heterostructure formed by two nanocrystals with different Fermi levels will generate a built-in electric field at the heterointerfaces, in which the electron transport was accelerated [27]. Sulfur species are believed to undergo continuous trapped-diffusion-conversion process across heterogeneous interfaces; LiPSs are rapidly trapped by high polar surface and then diffused across the interfaces followed by being reduced to solid-state Li_2S on the conductive and catalytic surface [21]. Although heterostructure catalysts have been widely used in LSBs, few studies on the interfacial adsorption energy to LiPSs. The inherent influence of heterogeneous interface on Li_2S deposition behavior during the redox process is necessary to further research.

The formation of Li_2S approximately accounts for three-quarters of the theoretical capacity during the discharge process in prevailing ether-based electrolytes [28]. However, the forming process of solid Li_2S from liquid LiPSs is considered as the rate-determining step in the redox process [29]. Moreover, the liquid-solid conversion product Li_2S may cover the catalysts surface, block down the charge transfer and ion diffusion and thus restrain the subsequent deposition process. Hence, it is crucial to facilitate the liquid-solid conversion and tune the growth of discharge product Li_2S to avoid the fast passivation of electrocatalysts for improving the overall performance. The forming of crystal nucleus usually preferentially takes place at the sites with high activity, while the heterogeneous interface is usually the highly active sites in the field of catalysis. So it is worth studying the influence of the high defect characteristics of the heterogeneous interface on the nucleation of Li_2S.

Monoclinic MoO_2 is a transition metal oxide with a twisted rutile crystal structure. The calculated energy band structure of MoO_2 shows that there are four Mo 4d bands lie below the Fermi energy, endowing it semi-metallic property [30]. Molybdenum carbides have been demonstrated a promising HER electrocatalyst due to the similar D-band electronic structure with the Pt-group metals [31]. The *FCC* α-MoC with better electronic conductivity than orthorhombic Mo_2C has been widely used in water-gas shift, hydrogen production reactions and other fields [32,33]. Both MoO_2 (8.8×10^{-5} Ω cm) and α-MoC (4.9×10^{-6} Ω cm) possess promising conductivity and polarity, showing great potential as LiPSs immobilizers and catalysts for the conversion reaction [34,35].

In this work, MoO_2 and α-MoC with similar low electrical resistivity were adopted to construct a heterostructure MoO_2/α-MoC catalyst for investigating the influence of heterointerfaces on the redox process of sulfur species and Li_2S deposition behavior. The minor difference in electronic conductivity makes it differs from the traditional trapping-diffusion-conversion model. DFT calculation results further revealed that the MoO_2/α-MoC heterogeneous interface show stronger affinity to LiPSs and its discharge products Li_2S than MoO_2 and α-MoC, which is conducive to facilitating the subsequent conversion process and inducing the heterogeneous nucleation and spatial precipitation of Li_2S. Therefore, the MoO_2/α-MoC heterointerface can not only effectively facilitate Li-ion diffusion and charge transfer but also provide adsorption and catalyzing sites for sulfur species [36], thereby improving the redox kinetics of sulfur species and simultaneously facilitating the LiPSs conversion. By introducing a small amount of MoO_2/α-MoC catalyst in the cathode, the cells reached a high capacity of 1177 mAh g^{-1} at 0.2 C and 695 mAh g^{-1} at 3 C. Moreover, by employing MoO_2/α-MoC functional interlayer, cells with high sulfur loading cathodes (5.0 mg cm^{-2}) and low electrolyte (6–7 μL mg^{-1}) showed stable cycling performance, achieving 829 mAh g^{-1} and a capacity retention of 85% after 100 cycles at 0.5 C. This work provides an understanding of accelerating the redox conversion process and promoting the Li_2S deposition behavior by constructing the two-dimensional heterogeneous interface.

2. Experimental section

2.1. Preparation of precursor $Mo_3O_{10}(C_6H_8N)_2{\cdot}2H_2O$ nano-rods

Typically, 1 mmol ammonium molybdate tetrahydrate ($(NH_4)_6Mo_7O_{24}{\cdot}4H_2O$) was dissolved in 60 mL deionized water, then 18 mmol aniline ($C_6H_5NH_2$) was added into the above solution under vigorous stirring. Then 1 M dilute hydrochloric acid was added dropwise to the solution until white precipitate appeared. The above mixed solution was heated in an oil bath at 50 °C for 4 h under continuous stirring. The precipitation was harvest by centrifugation and washed with ethanol and deionized water several times followed by drying at 70 °C under vacuum for 12 h.

2.2. Preparation of MoO_2, MoO_2/α-MoC and α-MoC nano-rods

The as-synthesized $Mo_3O_{10}(C_6H_8N)_2{\cdot}2H_2O$ precursor were put in the crucible and transferred to the tube furnace, then the tube furnace was vacuumed and argon was introduced to expel the air in the tube. The sample was annealed under different temperature of 600 °C, 650 °C and 700 °C for 4 h at the heating rate of 5 °C min^{-1} to synthesis MoO_2, MoO_2/α-MoC and α-MoC nano-rod, respectively.

2.3. Preparation of the graphene/sulfur composite

Graphene powder was prepared by freeze-drying a graphene oxide dispersion solution in water (1 wt%, The Sixth Element (Changzhou) Materials Technology Co., Ltd.) and then thermally treated at 900 °C under a pure Ar atmosphere for 2 h [8]. To gain graphene/sulfur composite: graphene and sublimed sulfur (1:3, wt./wt.) were homogenously grinded in a mortar and heated at 155 °C for 24 h under Argon protection.

2.4. Preparation of Li_2S_6 solution and symmetric cells tests

Sublimed sulfur and Li_2S powder (with molar ratio of 5:1) were added into a mixture of 1, 3-dioxolane (DOL)/dimethoxyethane (DME) (1:1, v/v) and stirred at 60 °C for 12 h in glovebox to obtain 0.2 M Li_2S_6 solution. Then the brown solution was diluted to 2 mM with DOL/DME for the polysulfide adsorption test. Li_2S_6-based symmetric cells were assembled using two identical CP electrodes loaded with sample (CP/MoO_2, CP/α-MoC, and CP/MoO_2/α-MoC) and 25 μL Li_2S_6-electrolyte (0.2 M) was added on both sides. CV was measured within a voltage range from −-0.8 to 0.8 V at scan rate of 10 mV s^{-1}.

2.5. Preparation of Li_2S_8 solution and Li_2S deposition/dissolution tests

Li_2S_8 solution was prepared by mixing a suitable amount of sulfur and Li_2S in a mixed solution of 1 M LiTFSI in DOL/DME (1:1, v/v) under vigorous mixing at 70 °C for 12 h. Commercial carbon paper (CP) was cut into disks and were used as substrates to load the samples. The samples were firstly ultrasonic treated in ethanol for 30 min and then loaded on the CP with areal loading of ~2.5 mg cm^{-2}. The cells were assembled using CP loaded with the samples as the cathode, lithium foil as anode and Celgard 2400 membrane as the separator. 25 μL Li_2S_8 solution was added on the cathode side and 25 μL blank electrolyte was added on the anode side. For the deposition test, the cells were firstly galvanostatic discharged (0.134 mA) until the voltage reached 2.10 V to convert high-order lithium polysulfide (Li_2S_8/Li_2S_6) to lower-order lithium polysulfide Li_2S_4, followed by potentiostatic discharging at 2.09 V until the current density decreased to 10^{-2} mA for the nucleation and precipitation of Li_2S. For the dissolution test, the above assembled cells were first galvanostatically (0.134 mA) discharged to 1.80 V

followed by potentiostatically discharge at 1.80 V until the charge current was below 10^{-2} mA. Then, the cells were charged at 2.40 V potentiostatically for the oxidization of Li_2S to LiPSs.

2.6. Electrochemical measurements

The cathode was fabricated by mixing graphene/sulfur composite (80 wt%), MoO_2, α-MoC or MoO_2/α-MoC (5 wt%), Super P (5 wt%) and poly(vinylidene fluoride) (10%) in N-methylpyrrolidone (NMP) to generate a homogeneous slurry. The slurry was coated onto Al foil and dried under vacuum at 60 °C overnight. The areal loading of sulfur in cathode was around 1–1.2 mg cm^{-2}. CR-2032 coin-type cells were assembled in an argon-filled glove box by using the as-prepared cathodes, lithium foil, Celgard 2400 membrane separator, and 1 M LiTFSI dissolved in DOL/DME (1:1, v/v) with 2 wt% $LiNO_3$ as electrolyte. The ratio of electrolyte to sulfur was 15 μL mg^{-1} for normal cathodes and 6–7 μL mg^{-1} for high sulfur loading cathodes.

Galvanostatic charge/discharge (GCD) measurements, rate and cycling performance of the coin cells were measured using Land CT2001A multichannel battery testing system with a voltage window of 1.7–2.8 V. Cyclic voltammetry (CV) and electrochemical impedance spectroscopy (EIS) measurements were performed with an electrochemical workstation (Gamry, interface 1000, Germany) at a scan rate of 0.1 mV s^{-1} and frequency range of 10 MHz to 0.01 Hz.

3. Results and discussion

3.1. Structure and morphology

The synthesis process of MoO_2/α-MoC heteronano-rod was illustrated in Fig. 1a. Organic-inorganic hybrid precursor $Mo_3O_{10}(C_6H_8N)_2{\cdot}2H_2O$ (Fig. S1) were prepared by a co-precipitation method, and then annealed in argon to form MoO_2, MoO_2/α-MoC and α-MoC nano-rods at 600 °C, 650 °C and 700 °C, respectively. Fig. 1b displays the XRD patterns of MoO_2, α-MoC and MoO_2/α-MoC. Diffraction peaks at 2θ=26.1° can be ascribed to the ($\bar{1}$11) plane of monoclinic MoO_2. As the annealing temperature rised to 650 °C, the peaks at 37.7°, 42.2° of the *FCC* α-MoC (111) and (200) plane appeared, indicating the co-existence of α-MoC (JCPDS no. 65-0280) and monoclinic MoO_2 (JCPDS no. 76-1807). After annealing at 700 °C, MoO_2 disappeared and α-MoC was harvested. The slight peak at 39.5° could be ascribed to orthorhombic Mo_2C. As the temperature increased to 710 °C, the (101) peak of Mo_2C becomes stronger (Fig. S2), suggesting more Mo_2C is formed at high temperatures. Thermogravimetric analysis (TGA) was performed to analyze the composition of MoO_2/α-MoC. Considering that both molybdenum dioxide and molybdenum carbide exist in the highest oxidation state (MoO_3) after calcination in air, the mass ratio of MoO_2, α-MoC and carbon was calculated to be 41.6: 54.3: 4.1 (Fig. S3) [37]. Scanning electron microscopy (SEM) images present that the nano-rods morphologies remained similar to the precursor during the carbonization process and formed rough nano-rods with several micrometers length and few tens of nanometers diameter, as shown in Fig. 1c. The periodic alternating assembly of MoO_4^{2-} and aniline in the precursor nano-rods ensures the uniform distribution of Mo species and carbon matrix, and further prohibits the excessive growth and aggregation of the nanocrystallines during the in situ carbothermal reduction [38]. Transmission electron microscopy (TEM) images further confirm that the nano-rods morphologies composed of the ultrasmall and highly dispersed particles (Fig. S4). High-resolution transmission electron microscopy (HRTEM) with selected area electron diffraction (SAED) was employed to confirm the formation of nanocrystal MoO_2 and α-MoC. The lattice fringes with 0.34 nm for MoO_2 ($\bar{1}$11) plane and 0.207 nm for α-MoC (200) plane were observed, and the formation of MoO_2/α-MoC interface was also marked in Fig. 1d. Unlike the general heterostructure that possesses a sharp interface, the interface between MoO_2 and α-MoC is less well defined, suggesting possible rich defects. In this case, the Electron Paramagnetic Resonance (EPR) spectrometer was employed to verify the surface defects (Fig. S5). The signal at g=2.0035 further demonstrates the existence of oxygen vacancies in MoO_2/α-MoC[39]. The energy-dispersive spectrometry (EDS) mapping displays the uniform distribution of Mo, C and O elements on an individual heteronano-rod (Fig. 1e). Briefly, MoO_2 and α-MoC nanocrystals are

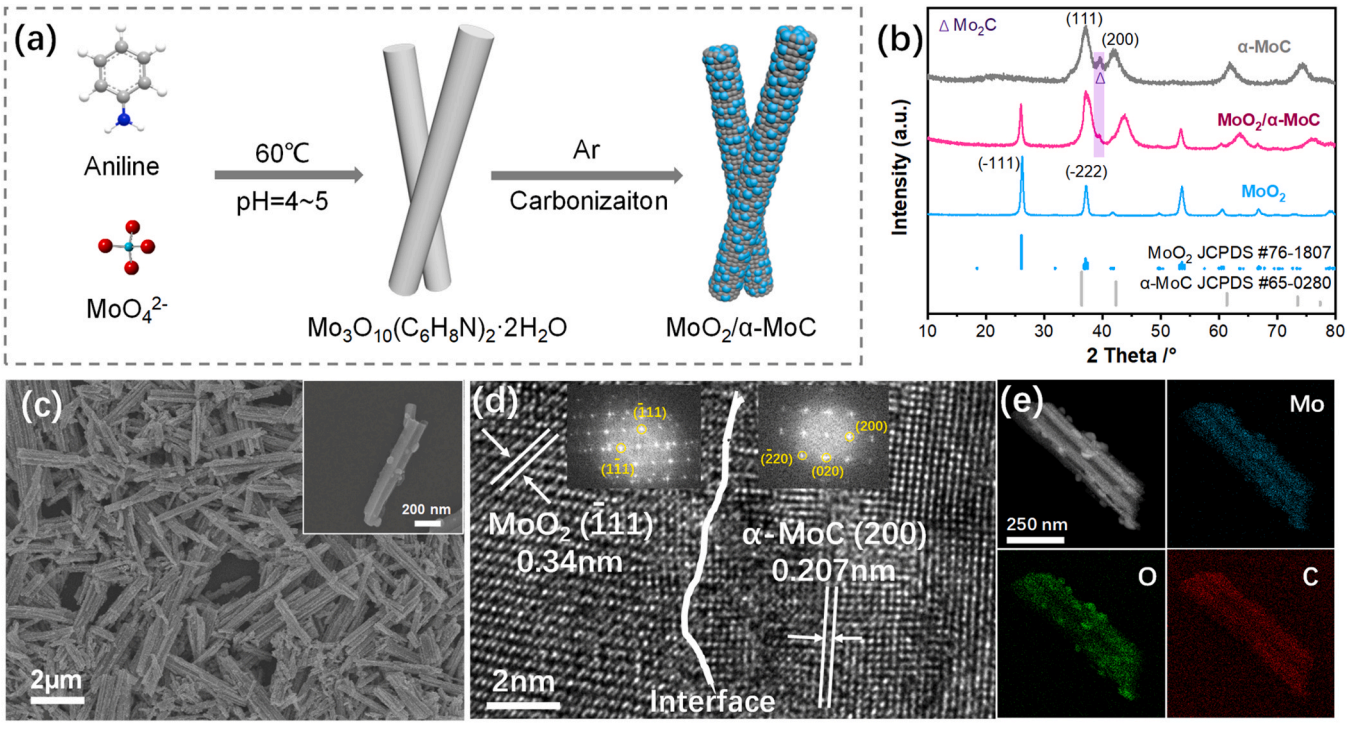

Fig. 1. (a) Schematic illustration of the synthetic process of MoO_2/α-MoC heterostructure. (b) XRD patterns of MoO_2, MoO_2/α-MoC and α-MoC. (c) SEM images MoO_2/α-MoC. (d) HRTEM and SEAD images of MoO_2/α-MoC and (g) TEM and corresponding elemental mapping images of Mo, C and O.

successfully integrated and formed a heterostructure.

3.2. Conversion kinetics of LiPSs

Adsorption of LiPSs on the catalyst surface is required for inhibiting the shuttle effect and catalyzing the redox process. Fig. 2a shows that commercial Super P, MoO_2, α-MoC and MoO_2/α-MoC were separately soaked into the solution of DOM/DME containing 2 mM Li_2S_6. After holding for 12 h, the color of the solution soaked with Super P remained almost unchanged, whereas the solutions with MoO_2, MoO_2/α-MoC and α-MoC present apparent decolorization, indicating the strong interaction with LiPSs. X-ray photoelectron spectroscopy (XPS) was conducted to investigate the interaction between MoO_2/α-MoC and LiPSs before and after the adsorption test. As shown in Fig. 2b, the high-resolution Mo 3d XPS spectrum reveals the signals of Mo–C and Mo–O bonding (also shown in Fig. S6). Mo–C bonding in α-MoC exhibits the $3d_{5/2}$ and $3d_{3/2}$ peaks located at 228.7 eV and 231.7 eV, respectively, in accordance with the literature data [40]. The Mo–O bonding exhibits three couple peaks, the doublet at 229.6 eV and 233 eV belongs to $3d_{5/2}$ and $3d_{3/2}$ of Mo^{4+} in MoO_2, respectively [22]. Besides, the doublet at 232.6 eV and 235.8 eV can be ascribed to Mo^{6+} resulted from surface oxidation of MoO_2. The doublet at 230.7 eV and 234.2 eV can be attributed to Mo^{5+}, which forms by the reduction of MoO_4^{2-} in the carbonization process. After soaking MoO_2/α-MoC in Li_2S_6 solution, both Mo–C and Mo–O bonds exhibit an obvious shift to the lower binding energy. The shift arises from the electrons around negative charged S atoms of sulfur species deviated to Mo sites, thus decreasing the binding energy of Mo atoms while increasing that of S atoms [11]. In the S 2p spectrum (Fig. S7), apart from the peak of Mo–S bonding located at 161.3 eV, the signals of S_B^0 at 164.7 eV and S_T^{-1} at 162.4 eV can also be detected, which show positive shifts comparing to pure Li_2S_6 [11]. Briefly, XPS spectra reveal the strong interaction between Mo atoms in MoO_2/α-MoC heteronano-rods and S atoms in sulfur species with the formation of Mo-S bond, which is in agreement with the result of visualized Li_2S_6 adsorption test.

DFT calculations were performed to simulate the adsorption of sulfur species on different surfaces at the atomic-level horizon. MoO_2 and α-MoC were simulated by slab models of the ($\bar{1}$11) and (200) surfaces, respectively. The optimized geometries of sulfur species (S_8, Li_2S_8, Li_2S_6, Li_2S_4, Li_2S_2 and Li_2S) adsorption on the surface of MoO_2 ($\bar{1}$11), α-MoC (200) and MoO_2/α-MoC heterointerface are exhibited in Fig. S8 and the calculated adsorption energies are summarized in Fig. 2c. Chemisorption of the sulfur species is mainly enabled by the formation of Mo–S bond between sulfur species and MoO_2, α-MoC or MoO_2/α-MoC heterointerface, which is consistent with the XPS results. The calculated adsorption energies for soluble Li_2S_8, Li_2S_6 and Li_2S_4 at the interface are −2.88 eV, −2.64 eV and −2.55 eV, respectively, which are higher than that for MoO_2 (−1.1 eV, −1.32 eV, −0.98 eV) and α-MoC (−2.13 eV, −2.14 eV, −2.3 eV). The superior adsorption ability of heterointerface indicates that the strong chemisorption of soluble LiPSs can inhibit its shuttling, which is essential for facilitating the subsequent conversion process. Especially, the heterointerface also shows the strongest adsorption toward discharge products Li_2S_2 and Li_2S, which is conducive to the nucleation process.

To verify the positive effect of MoO_2/α-MoC on the LiPSs redox kinetics, symmetrical cells were assembled using different samples loaded on carbon paper (CP) as electrodes and 0.2 M Li_2S_6 as electrolyte and tested within a voltage range of −0.8 to 0.8 V at 10 mV s^{-1} scan rate. As shown in Fig. 2d, the cyclic voltammetry curves of symmetrical cells with MoO_2/α-MoC exhibit greater redox current response and smaller voltage separation than that of MoO_2 and α-MoC, confirming the boosted redox kinetics of LiPSs conversions in the presence of MoO_2/α-MoC.

3.3. Deposition behavior of Li_2S

The reduction of sulfur involves a multistep solid-liquid-solid transformation accompanied by Li-ion and electron migration, with forming solid-state insulating lithium sulfide (Li_2S) as the final lithiation product on the surface of substrates. To investigate the Li_2S nucleation behavior on the surface of MoO_2, α-MoC and MoO_2/α-MoC, Li_2S precipitation tests were conducted by employing Li_2S_8-containing catholyte and the recorded current-time (i-t) response curves were depicted in Fig. 2e

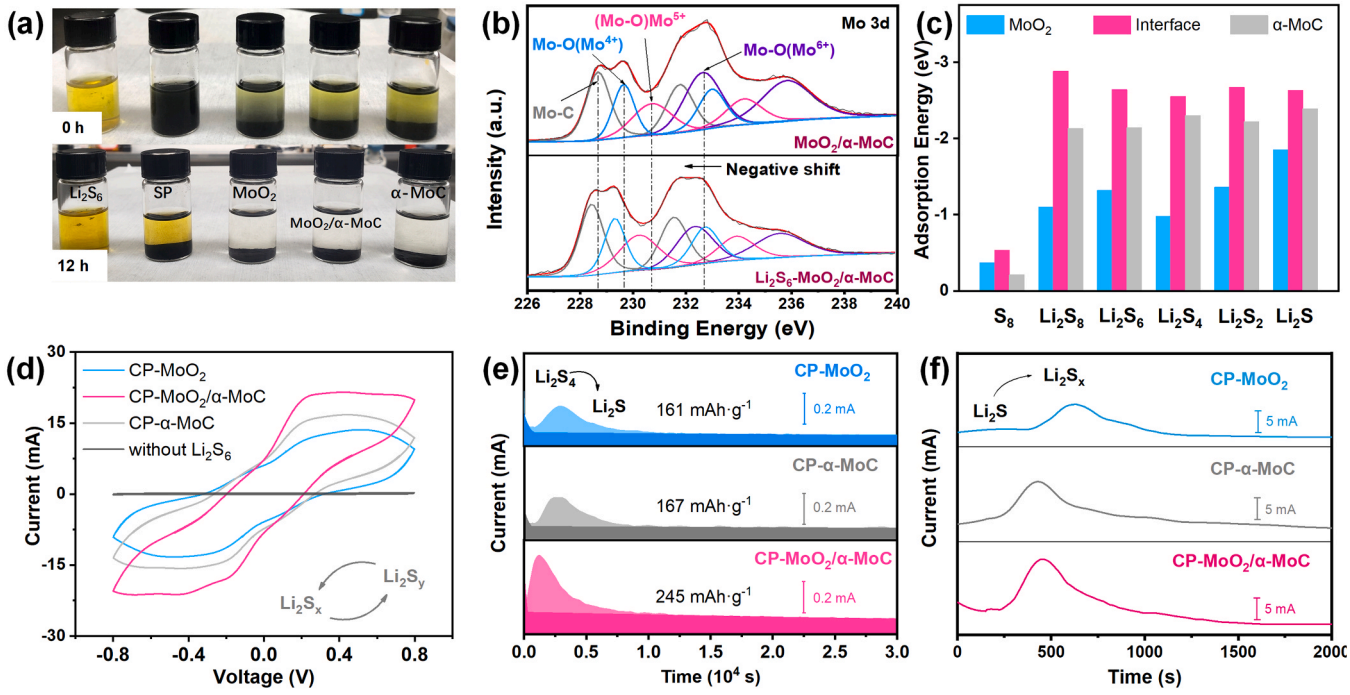

Fig. 2. (a) Photographs of Li_2S_6 solutions without and with Super P, MoO_2, MoO_2/α-MoC and α-MoC just added and after 12 h. (b) Mo 3d and (c) adsorption energies of sulfur species on MoO_2 ($\bar{1}$11), α-MoC (200) and the heterointerface. (d) CV profiles of symmetric cells at a scan rate of 10 mV s^{-1}. (e) Potentiostatic discharge i-t profiles at 2.09 V on different samples. (f) Potentiostatic charge i-t profiles at 2.40 V on different samples for evaluation of Li_2S dissolution behavior.

[41]. The capacities of Li_2S precipitation on MoO_2, α-MoC and MoO_2/α-MoC are calculated to be 160, 167 and 245 mAh g^{-1}, respectively. The difference in precipitation capacities indicates that MoO_2/α-MoC is conducive to facilitating the liquid-solid phase transformation (Li_2S_4–Li_2S) during the electrochemical process [15]. For the Li_2S dissolution process (Fig. 2f), the oxidation response current was higher for MoO_2/α-MoC electrodes than that of MoO_2 and α-MoC electrodes, suggesting the catalytic activity of MoO_2/α-MoC on Li_2S oxidation process [26]. SEM images show that a few Li_2S deposits still exist on MoO_2 surface after dissolution process (Fig. S9). In contrast, the MoO_2/α-MoC and α-MoC show clean surfaces without Li_2S deposits on it, ensuring that the electrocatalyst maintaining catalytic activity during cycling.

To further reveal the kinetic characteristics of Li_2S deposition on different surfaces, the dimensionless current-time transient curves obtained from potentiostatic discharge results are recorded and fitted with the four classical models of electrochemical deposition: 2DI and 2DP represent the two-dimensional (2D) instantaneous (I) or progressive (P) nucleation modes, in which the crystallite growth is further controlled by the lattice incorporation. 3DI and 3DP represent the three-dimensional (3D) instantaneous (I) or progressive (P) nucleation of the hemispherical nucleus, with the growth rate controlled by ion diffusion [42] (Eq. (S2)). The deposition morphology of Li_2S on different samples were further observed by SEM after potentiostatic discharge (Fig. 3 and Fig. S10). It can be clearly observed in Fig. 3a–c that the Li_2S precipitation process on MoO_2 and α-MoC surfaces match well with the 2D precipitation model. As previously reported, the time when the maximum current (I_m) occurs can reflect the moment Li_2S nucleus coalesce and form a two-dimensional thin film [41]. To more deeply observe the evolution of the Li_2S morphology during the deposition process, the cells were stopped and disassembled as soon as the current response reaches I_m, followed by characterizing the electrode by SEM (Fig. 3d–f). It can be clearly observed that the MoO_2 and α-MoC surface were covered by smooth Li_2S thin layers, indicating the rapid surface passivation and relatively weak solution-mediated Li_2S growth. In contrast, the MoO_2/α-MoC surface was covered by rough and dense Li_2S particles owing to the promoted solution-mediated growth pathway. After potentiostatic discharging, a dense film-type Li_2S layer was formed and covered on the MoO_2 (Fig. 3g) and α-MoC (Fig. 3h) surface. In this cases, the MoO_2 and α-MoC provide contiguous two-dimensional nucleation sites for Li_2S precipitation, enabling the rapid formation of film-type Li_2S layer. Specifically, Li_2S first randomly nucleated on the surface of MoO_2 or α-MoC, forming abundant growth sites, and the good intrinsic conductive nature of both MoO_2 and α-MoC allow the relatively fast lateral growth of Li_2S. Therefore, new Li_2S forms at the triple-phase boundary between the existing Li_2S nucleus, conductive MoO_2 (or α-MoC) substrate and the electrolyte, end up in the formation of a two-dimensional film-like Li_2S precipitation layer. However, the insulating Li_2S layer may lead to rapid passivation of the surface and result in poor reaction kinetics, thus impeding the subsequent Li_2S deposition, as illustrated in Fig. 4a and b [43]. Interestingly, the electrodeposition behavior of Li_2S on MoO_2/α-MoC deviates the 2D models and shows a tendency to obey the 3D progressive nucleation model (Fig. 3c). As for the conventional DOL/DME solvent system, in 2DP and 2DI models, the

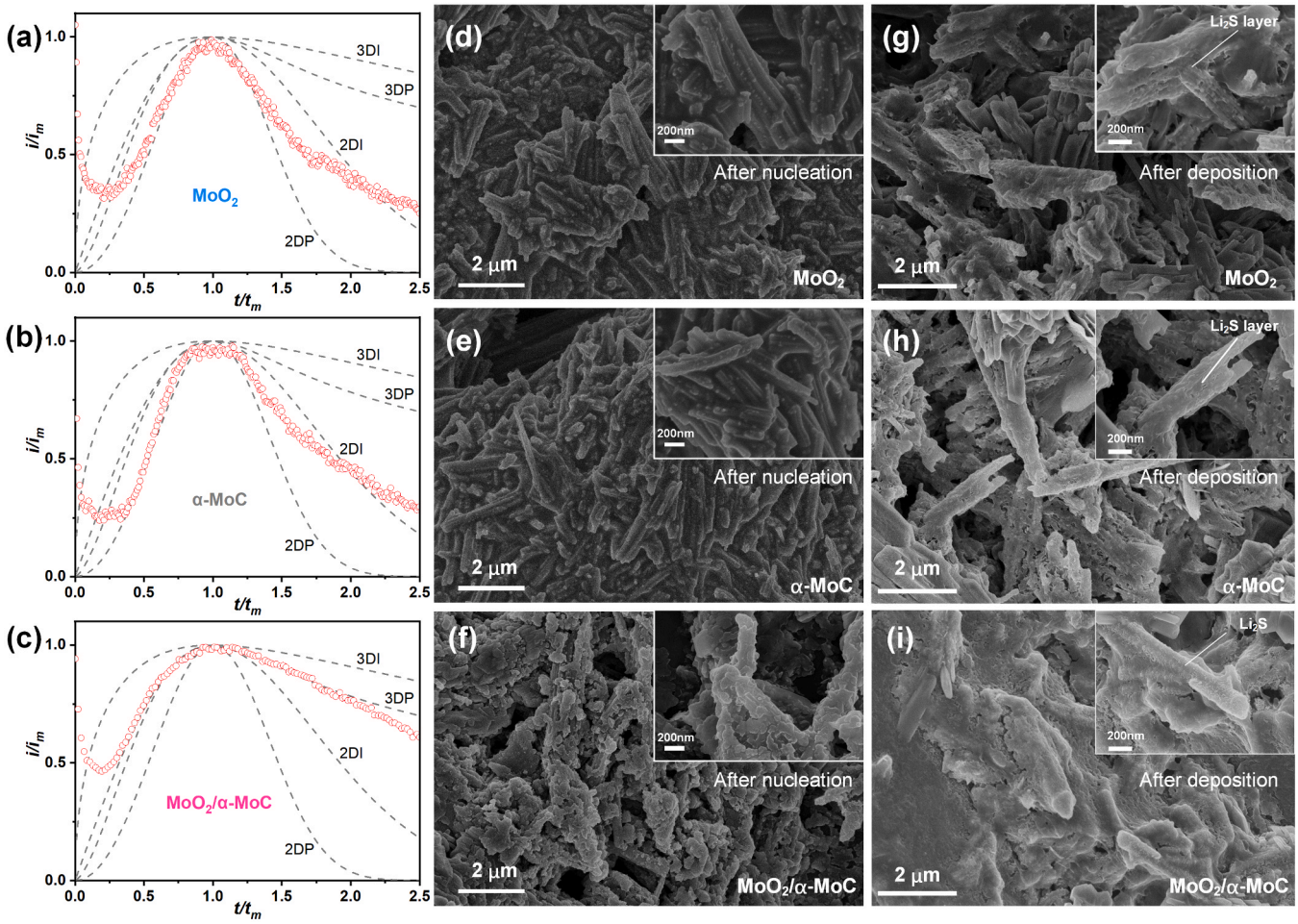

Fig. 3. Dimensionless transient profiles of (a) MoO_2, (b) α-MoC and (c) MoO_2/α-MoC at 2.09 V. SEM images of MoO_2, α-MoC and, MoO_2/α-MoC electrodes after discharged to I_m (d–f) and after Li_2S deposition (g–i).

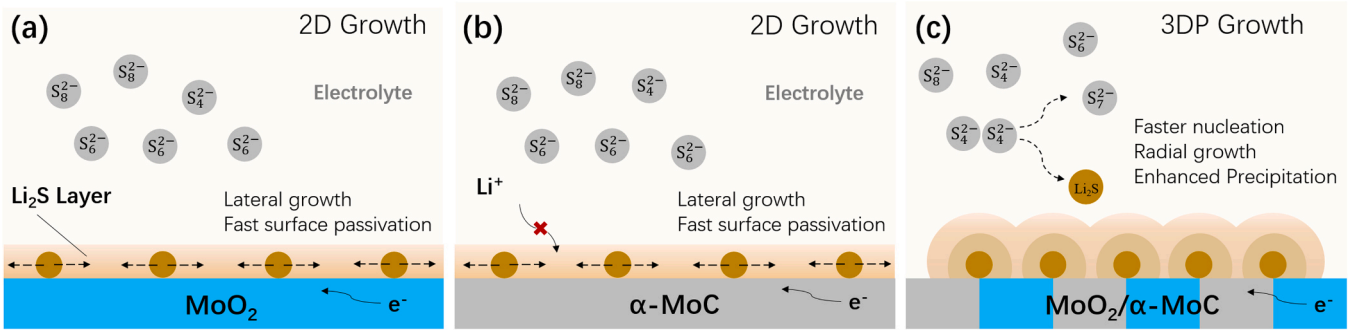

Fig. 4. Schematic illustration of the Li_2S deposition process on the surface of MoO_2, α-MoC and MoO_2/α-MoC.

growth was controlled by the incorporation between the adatoms and lattice interface, while the growth was controlled by volume diffusion in 3DI and 3DP [42,44]. Apparently, the 3DP mode suggests that the Li_2S precipitation behavior was controlled by both lateral atomic diffusions at the heterogeneous interfaces and the ion transportation in the electrolyte (Fig. 4c) [45]. Since the reduction of long-chain LiPSs can be promoted at the heterointerfaces, the reactant (S_4^{2-}) for the typical disproportional reaction ($2S_4^{2-} \rightarrow S_2^{-} + S_7^{2-}$) are abundant near the surface with less Li_2S_{6-8} left, the solution-mediated growth of Li_2S can be significantly promoted with the aid of MoO_2/α-MoC. Apart from the lateral growth at the triple-phase boundary, radial precipitation can be achieved at the same time through solution-mediated growth, further bringing about the 3D Li_2S coverage [46]. Correspondingly, SEM images showed that the continuous thick Li_2S layer fully covered the MoO_2/α-MoC surface and the gap between the heteronano-rods after potentiostatic discharging, suggesting higher Li_2S precipitation capacity than that on MoO_2 and α-MoC (Fig. 3i).

The above results suggest that the heterogeneous interfaces of MoO_2/α-MoC can not only accelerate the Li_2S nucleation due to the strong interaction between the heterointerfaces and LiPSs but also facilitate the radial growth of Li_2S by improving the mass transportation in the electrolyte, thus lead to three-dimensional Li_2S precipitation.

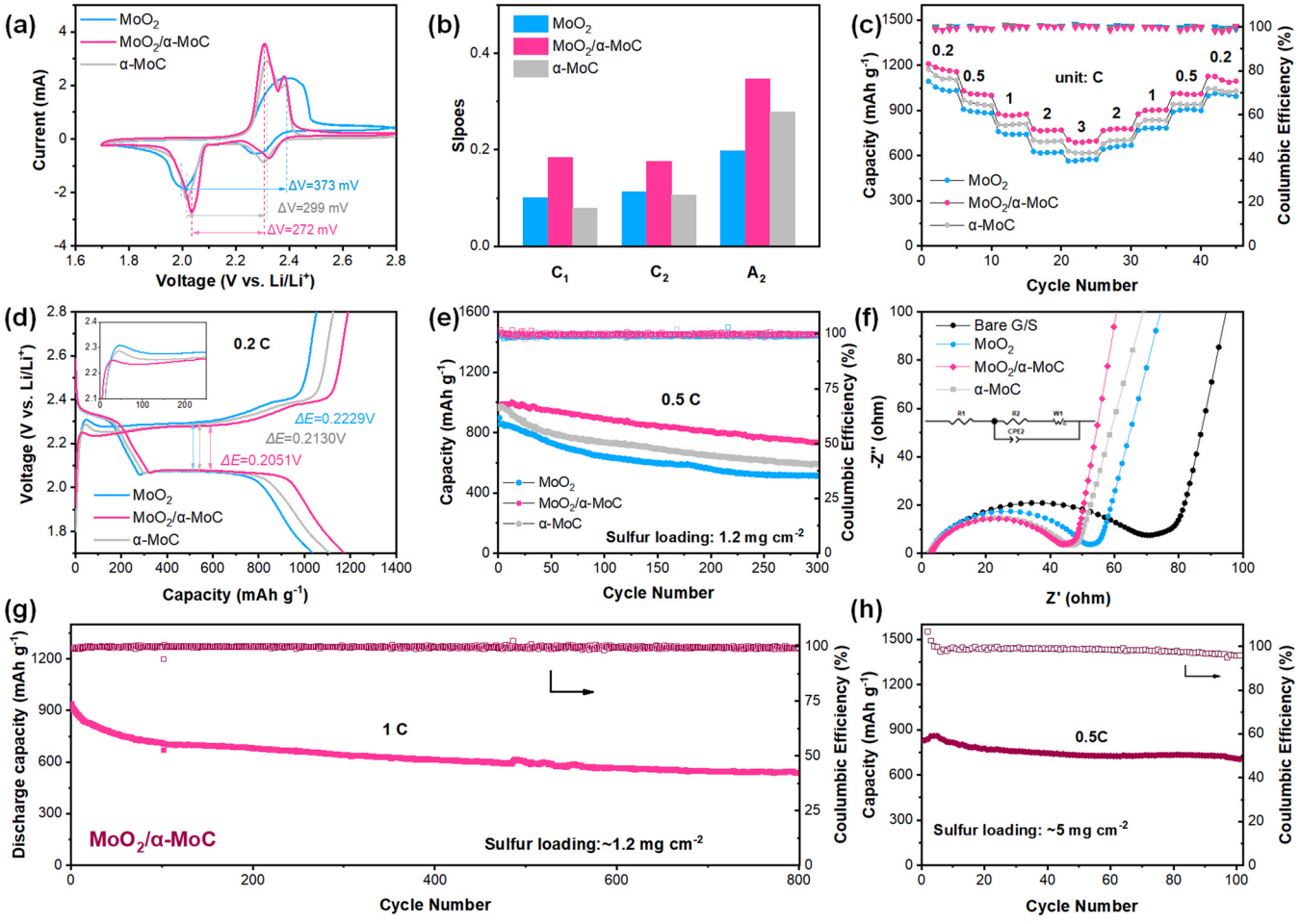

Fig. 5. Electrochemical performance of Li-S batteries. (a) CV profiles at 0.1 mV s^{-1}. (b) slopes of fitted lines for CV peak currents versus square root scan rates. (c) Rate performance. (d) Comparing the potential polarizations (ΔE) of the cathodes with different additives in charge/discharge profiles at 0.2 C. (e) Cycling performance at 0.5 C. And (f) EIS curves of cells before cycling. (g) Long-term cycling for the cathodes with MoO_2/α-MoC at 1 C for 800 cycles and (h) cycling performances of the cells with MoO_2/α-MoC interlayer at high areal sulfur loading.

3.4. Electrochemical properties and battery performance

To systematically evaluate the influence of introducing the samples as additives without decreasing battery capacity, cathodes containing 5 wt% additives were prepared and assembled in CR2032 coin cells. Fig. 5a displays the profiles of the cells within the voltage window of 1.7–2.8 V (versus Li/Li^+) at a scan rate of 0.1 mV s^{-1}. In the cathodic scan process, all cells display two cathodic peaks which can be ascribed to the reduction of S_8 to high-order LiPSs (C1), and the subsequent reduction of LiPSs towards solid-state Li_2S_2/Li_2S (C2), respectively. In the subsequent anodic scan, the characteristic peaks stem from the reversible oxidation of Li_2S_2/Li_2S to LiPSs (A1), and subsequently to S_8 (A2). The potential differences (ΔV) between the second cathodic peak (LiPSs-Li_2S_2/Li_2S) and the major anodic peak are also compared and marked. For the cells with MoO_2/α-MoC, the ΔV (272 mV) was significantly lower than that of α-MoC (299 mV) and MoO_2 (373 mV). Moreover, the cells with MoO_2/α-MoC show the greater current response, indicating the effectively improved conversion kinetics and reduced overpotential during the redox process [24]. For the cells with α-MoC and MoO_2/α-MoC, the oxidation process of Li_2S was kinetically improved, resulting in narrower peaks with higher current response and the obvious peak separation during the anodic scan. The oxidation peaks significantly shifted to lower voltage. In comparison, MoO_2 show a relatively limited effect on the kinetic improvement of the Li_2S oxidation process and exhibit the lowest current response and a broad anodic peak at around 2.39 V.

In electrochemical reversible systems (the potentials and concentrations follow the Nernst equation or its derived equations), the cathodic and anodic peak current (I_p) can be described by the Randles–Sevick equation and the slope of linear curves reflects the Li-ion diffusivity (Eq. (S1)) [47]. Therefore, CV tests of cells with different additives were carried out at an increased scan rate from 0.1 to 0.5 mV s^{-1} (Fig. S11). As summarized in Fig. 5b, the curve slopes of the cells with MoO_2/α-MoC are larger than that of cells with MoO_2 or α-MoC in both oxidation and reduction processes, illustrating the faster Li^+ diffusion. Notably, cells with MoO_2/α-MoC exhibit larger slope in the oxidation process of Li_2S, indicating the faster decomposition of solid-state Li_2S on the surface of MoO_2/α-MoC.

As presented in Fig. 5c, the cells with MoO_2/α-MoC deliver higher capacity at various current densities (from 0.2 to 3 C) than cells with MoO_2 and α-MoC. The cell with MoO_2/α-MoC exhibits a significant high specific capacity of 1177 mA h g^{-1} at 0.2 C (1 C=1675 mA g^{-1}), which is higher than α-MoC (1125 mAh g^{-1}) and MoO_2 (1050 mAh g^{-1}). At further increased current densities, the MoO_2/α-MoC-containing cells still deliver high specific capacities of 1011 and 872, 770 and 695 mAh g^{-1} at 0.5, 1, 2 and 3 C, respectively. When the current density was gradually returned to 0.2 C, the specific capacities of the cells recovered to a similar level of the initial process, demonstrating the superior electrochemical reversibility of the cells at high current density. Typical charge/discharge plateaus, which are in good agreement with the results of CV measurements, were clearly observed in the charge and discharge profiles (Fig. S12). The characteristic plateaus can still be clearly observed even under the high rate of 3 C, signifying the excellent redox kinetics of sulfur species in MoO_2/α-MoC-containing cells at high current density.

The galvanostatic charge and discharge profiles of cells with different additives at 0.2 C in the second cycle were compared in Fig. 5d. The capacity difference between the charge and discharge process can be ascribed to the rearrangement of sulfur and the incomplete conversion between long-chain LiPSs and the final discharge products Li_2S, which leads to the inevitable shuttle of active substances[48]. The cells with MoO_2/α-MoC exhibit longer discharge plateaus and smaller voltage hysteresis (ΔE=0.2051 V) than cells with α-MoC (ΔE=0.2140 V) and MoO_2 (ΔE=0.2229 V), indicating the fastest conversion kinetics of LiPSs. Additionally, the initial activation energy barriers of Li_2S on various additive materials were also compared and depicted insert Fig. 5d. The cells with MoO_2/α-MoC demonstrated a lower overpotential for the conversion of solid-state Li_2S to soluble LiPSs than cells with MoO_2 and α-MoC, which is indicative of the excellent catalytic effect on Li_2S activation at polysulfides and improve the sulfur utilization [24].

Cycling stability of cells with different additives was measured at 0.5 C, as shown in Fig. 5**e**. The cells with MoO_2/α-MoC exhibited the highest initial discharge capacity of 988 mAh g^{-1} at 0.5 C, exceeding that of cells with α-MoC (959 mAh g^{-1}) and MoO_2 (897 mAh g^{-1}). After 300 cycles, a high capacity of around 735 mAh g^{-1} with high Coulombic Efficiency of over 99.8% can still be maintained. In contrast, cells without additives exhibited an initial discharge capacity of 760 mAh g^{-1} at 0.5 C and rapidly decay to 508 mAh g^{-1} after 300 cycles (Fig. S13). The lack of polar electrocatalysts leads to weak confinement and easy detachment of LiPSs as well as sluggish redox kinetics, further causing severe shuttle effect and rapid capacity decay. Galvanostatic charge and discharge profiles of cells with MoO_2/α-MoC for different cycles are depicted in Fig. S14. Obviously, the well-defined plateaus remained stable during cycling. The long-term cycling performance of the cells with MoO_2/α-MoC at high current density was also explored. As shown in Fig. 5g, the cells exhibit an initial discharge capacity of 935 mAh·g^{-1} and achieved a low-capacity decay of 0.053% per cycle after 800 cycles at a current density of 1 C. Electrochemical impedance spectroscopy (EIS) measurements before and after cycles are conducted and the results are depicted in Fig. 5f and Fig. S15. The fitted results show that the charge transfer resistance (Rct) of cells with MoO_2/α-MoC (39.4 Ω) was lower than that of cells with MoO_2 (47.2 Ω) or α-MoC (42.3 Ω) and pure G/S cathode (65.6 Ω). Moreover, the cells with MoO_2/α-MoC also show a smaller Rct (8.29 Ω) than MoO_2 (13.26 Ω), α-MoC (12.60 Ω) and G/S (18.74 Ω), indicating the accelerated charge transfer at the electrode surface and improved LiPSs conversion during redox process in the presence of MoO_2/α-MoC.

It should be noted that the above electrochemical tests were carried out at a relatively low sulfur loading (1–1.2 mg cm^{-2}) and an E/S ratio of ~15 μL mg^{-1}, which is not enough to meet the commercial needs [49]. The high E/S ratio may cause a large amount of LiPSs to dissolve in the electrolyte and reduce sulfur utilization. However, low E/S may lead to unstable Coulomb efficiency and shorten the cycle life of the cells. Therefore, it is critical for practical LSBs to obtain high and stable Coulombic efficiency under high sulfur loading and lean electrolyte conditions [50,51]. To this concern, cells with higher sulfur loading cathodes (~5 mg cm^{-2}) were prepared and the electrolyte volume/sulfur weight ratio was controlled at around 6–7 μL mg^{-1} for further investigation. MoO_2/α-MoC was coated on the separator as a functional interlayer. The cells with high sulfur loading cathode and interlayer were assembled and tested at 0.5 C current density to evaluate the cyclic performance (Fig. 5h). Briefly, the cells with MoO_2/α-MoC interlayer exhibit a relatively high discharge capacity of 829 mAh g^{-1} at 0.5 C. Even after 100 cycles, a discharge capacity of 710 mAh g^{-1} is maintained with high Coulombic Efficiency (>96%). Such desirable cycling performances under high sulfur loading and low electrolyte condition suggest the promising potential of MoO_2/α-MoC catalyst towards practical applications of Li-S batteries.

4. Conclusions

Heterostructure MoO_2/α-MoC as the electrocatalyst for lithium-sulfur batteries have demonstrated to effectively boost the LiPSs conversion kinetics and induce the high capacity precipitation of Li_2S. As two-dimensional defects, the heterogeneous interface with enhanced charge and mass transfer showed more favorable adsorption to sulfur species and catalytic activity for LiPSs redox process. More importantly, the heterogeneous interfaces provided advantageous nucleation sites and induced spatial precipitation (3DP growth) of Li_2S through accelerating the mass transportation in the electrolyte, leading to improved deposition capacity. By introducing MoO_2/α-MoC as additives in the sulfur cathode, the battery exhibits a greater discharge capacity at 0.5 C

before and after cycles than MoO_2 and α-MoC. Even with a high sulfur loading of 5.0 mg cm^{-2} and a low E/S ratio of 6–7 μL mg^{-1}, the battery with MoO_2/α-MoC functional interlayer also shows a high sulfur utilization and stable cycling performance at 0.5 C. This work provides a view of boosting the redox the conversion kinetics of LiPSs and promoting Li_2S deposition behavior by constructing the heterogeneous interface as the catalyst for lithium-sulfur batteries.

CRediT authorship contribution statement

Da-Qian Cai: Conceptualization, Investigation, Formal analysis, Writing – original draft. **Jin-Lin Yang**: Formal analysis, Writing – review & editing. **Ting Liu**: Formal analysis, Supervision. **Shi-Xi Zhao**: Project administration, Writing – review & editing, Supervision. **Guozhong Cao:** Writing – review & editing, Supervision.

Declaration of Competing Interest

The authors declare that they have no known competing financial interests or personal relationships that could have appeared to influence the work reported in this paper.

Acknowledgements

This work has been financially supported by the Shenzhen Basic Research Project Funds (JCYJ20190813172807127).

Appendix A. Supporting information

Supplementary data associated with this article can be found in the online version at doi:10.1016/j.nanoen.2021.106452.

References

[1] Y.-X. Yin, S. Xin, Y.-G. Guo, L.-J. Wan, Lithium-Sulfur batteries: electrochemistry, materials, and prospects, Angew. Chem. Int. Ed. 52 (2013) 13186–13200.
[2] A. Manthiram, Y. Fu, S.-H. Chung, C. Zu, Y.-S. Su, Rechargeable Lithium-Sulfur batteries, Chem. Rev. 114 (2014) 11751–11787.
[3] A. Manthiram, Y. Fu, Y.-S. Su, Challenges and prospects of Lithium-Sulfur batteries, Acc. Chem. Res. 46 (2013) 1125–1134.
[4] Z.W. Seh, Y. Sun, Q. Zhang, Y. Cui, Designing high-energy Lithium-Sulfur batteries, Chem. Soc. Rev. 45 (2016) 5605–5634.
[5] L. Ji, M. Rao, H. Zheng, L. Zhang, Y. Li, W. Duan, J. Guo, E.J. Cairns, Y. Zhang, Graphene oxide as a sulfur immobilizer in high performance Lithium/Sulfur cells, J. Am. Chem. Soc. 133 (2011) 18522–18525.
[6] S. Zhang, M. Zheng, Z. Lin, N. Li, Y. Liu, B. Zhao, H. Pang, J. Cao, P. He, Y. Shi, Activated carbon with ultrahigh specific surface area synthesized from natural plant material for Lithium-Sulfur batteries, J. Mater. Chem. A 2 (2014) 15889–15896.
[7] Z.-L. Xu, J.-K. Kim, K. Kang, Carbon nanomaterials for advanced Lithium Sulfur batteries, Nano Today 19 (2018) 84–107.
[8] L. Zhou, N. Ding, J. Yang, L. Yang, Y. Zong, Z. Liu, A. Yu, Sulfur encapsulated in Mo_4O_{11}-anchored ultralight graphene for high-energy Lithium Sulfur batteries, ACS Sustain. Chem. Eng. 4 (2016) 3679–3687.
[9] H. Lin, L. Yang, X. Jiang, G. Li, T. Zhang, Q. Yao, G.W. Zheng, J.Y. Lee, Electrocatalysis of polysulfide conversion by sulfur-deficient MoS_2 nanoflakes for Lithium-Sulfur batteries, Energy Environ. Sci. 10 (2017) 1476–1486.
[10] S. Huang, E. Huixiang, Y. Yang, Y. Zhang, M. Ye, C.C. Li, Transition metal phosphides: new generation cathode host/separator modifier for Li-S batteries, J. Mater. Chem. A 9 (2021) 7458–7480.
[11] G. Chen, Y. Li, W. Zhong, F. Zheng, J. Hu, X. Ji, W. Liu, C. Yang, Z. Lin, M. Liu, MOFs-derived porous Mo_2C-C nano-octahedrons enable high-performance Lithium-Sulfur batteries, Energy Storage Mater. 25 (2020) 547–554.
[12] Z. Xiao, Z. Li, X. Meng, R. Wang, MXene-engineered Lithium-Sulfur batteries, J. Mater. Chem. A 7 (2019) 22730–22743.
[13] J. He, A. Bhargav, A. Manthiram, Molybdenum boride as an efficient catalyst for polysulfide redox to enable high-energy-density Lithium-Sulfur batteries, Adv. Mater. 32 (2020), 2004741.
[14] H. Yuan, H.-J. Peng, J.-Q. Huang, Q. Zhang, Sulfur Redox Reactions at Working Interfaces in Lithium-Sulfur Batteries: A Perspective, Adv. Mater. Interfaces 6 (2019), 1802046.
[15] H. Ye, J. Sun, S. Zhang, H. Lin, T. Zhang, Q. Yao, J.Y. Lee, Stepwise electrocatalysis as a strategy against polysulfide shuttling in Li-S batteries, ACS Nano 13 (2019) 14208–14216.
[16] P. Wang, B. Xi, M. Huang, W. Chen, J. Feng, S. Xiong, Emerging catalysts to promote kinetics of Lithium-Sulfur batteries, Adv. Energy Mater. 11 (2021), 2002893.
[17] H. Lin, S. Zhang, T. Zhang, H. Ye, Q. Yao, G.W. Zheng, J.Y. Lee, Elucidating the catalytic activity of oxygen deficiency in the polysulfide conversion reactions of Lithium-Sulfur batteries, Adv. Energy Mater. 8 (2018), 1801868.
[18] H. Wang, W. Fu, X. Yang, Z. Huang, J. Li, H. Zhang, Y. Wang, Recent advancements in heterostructured interface engineering for hydrogen evolution reaction electrocatalysis, J. Mater. Chem. A 8 (2020) 6926–6956.
[19] Z. Hu, Q. Liu, S.-L. Chou, S.-X. Dou, Two-dimensional material-based heterostructures for rechargeable batteries, Cell Rep. Phys. Sci. 2 (2021), 100286.
[20] S. Huang, Z. Wang, Y. Von Lim, Y. Wang, Y. Li, D. Zhang, H.Y. Yang, Recent advances in heterostructure engineering for Lithium-Sulfur batteries, Adv. Energy Mater. 11 (2021), 2003689.
[21] T. Zhou, W. Lv, J. Li, G. Zhou, Y. Zhao, S. Fan, B. Liu, B. Li, F. Kang, Q.-H. Yang, Twinborn TiO_2-TiN heterostructures enabling smooth trapping-diffusion-conversion of polysulfides towards ultralong life Lithium-Sulfur batteries, Energy Environ. Sci. 10 (2017) 1694–1703.
[22] J.-L. Yang, S.-X. Zhao, Y.-M. Lu, X.-T. Zeng, W. Lv, G.-Z. Cao, In-situ topochemical nitridation derivative MoO_2-Mo_2N binary nanobelts as multifunctional interlayer for fast-kinetic Li-Sulfur batteries, Nano Energy 68 (2020), 104356.
[23] Z. Cao, J. Jia, S. Chen, H. Li, M. Sang, M. Yang, X. Wang, S. Yang, Integrating polar and conductive Fe_2O_3-Fe_3C interface with rapid polysulfide diffusion and conversion for high-performance Lithium-Sulfur batteries, ACS Appl. Mater. Interfaces 11 (2019) 39772–39781.
[24] L. Zhang, Y. Liu, Z. Zhao, P. Jiang, T. Zhang, M. Li, S. Pan, T. Tang, T. Wu, P. Liu, Y. Hou, H. Lu, Enhanced polysulfide regulation via porous catalytic V_2O_3/V_8C_7 heterostructures derived from metal-organic frameworks toward high-performance Li-S batteries, ACS Nano 14 (2020) 8495–8507.
[25] R. Fang, S. Zhao, Z. Sun, D.-W. Wang, R. Amal, S. Wang, H.-M. Cheng, F. Li, Polysulfide immobilization and conversion on a conductive polar MoC@MoO_x material for Lithium-Sulfur batteries, Energy Storage Mater. 10 (2018) 56–61.
[26] R. Wang, C. Luo, T. Wang, G. Zhou, Y. Deng, Y. He, Q. Zhang, F. Kang, W. Lv, Q.-H. Yang, Bidirectional catalysts for liquid-solid redox conversion in Lithium-Sulfur batteries, Adv. Mater. 32 (2020), 2000315.
[27] J. Ni, M. Sun, L. Li, Highly efficient sodium storage in iron oxide nanotube arrays enabled by built-in electric field, Adv. Mater. 31 (2019), 1902603.
[28] M. Zhao, H.-J. Peng, J.-Y. Wei, J.-Q. Huang, B.-Q. Li, H. Yuan, Q. Zhang, Dictating high-capacity Lithium-Sulfur batteries through redox-mediated lithium sulfide growth, small, Methods 4 (2020), 1900344.
[29] G. Xia, J. Ye, Z. Zheng, X. Li, C. Chen, C. Hu, Catalytic FeP decorated carbon black as a multifunctional conducting additive for high-performance Lithium-Sulfur batteries, Carbon 172 (2021) 96–105.
[30] D.O. Scanlon, G.W. Watson, D.J. Payne, G.R. Atkinson, R.G. Egdell, D.S.L. Law, Theoretical and experimental study of the electronic structures of MoO_3 and MoO_2, J. Phys. Chem. C 114 (2010) 4636–4645.
[31] X. Zhang, J. Wang, T. Guo, T. Liu, Z. Wu, L. Cavallo, Z. Cao, D. Wang, Structure and phase regulation in Mo_xC (α-MoC_{1-x}/β-Mo_2C) to enhance hydrogen evolution, Appl. Catal. B Environ. 247 (2019) 78–85.
[32] Y. Ge, X. Qin, A. Li, Y. Deng, L. Lin, M. Zhang, Q. Yu, S. Li, M. Peng, Y. Xu, X. Zhao, M. Xu, W. Zhou, S. Yao, D. Ma, Maximizing the synergistic effect of CoNi catalyst on α-MoC for robust hydrogen production, J. Am. Chem. Soc. 143 (2021) 628–633.
[33] L. Lin, Q. Yu, M. Peng, A. Li, S. Yao, S. Tian, X. Liu, A. Li, Z. Jiang, R. Gao, X. Han, Y.-w Li, X.-d Wen, W. Zhou, D. Ma, Atomically dispersed Ni/α-MoC catalyst for hydrogen production from methanol/water, J. Am. Chem. Soc. 143 (2021) 309–317.
[34] J. Liu, P. Wang, J. Fan, H. Yu, Carbon-coated cubic-phase molybdenum carbide nanoparticle for enhanced photocatalytic H_2-evolution performance of TiO_2, J. Energy Chem. 51 (2020) 253–261.
[35] X. Hu, W. Zhang, X. Liu, Y. Mei, Y. Huang, Nanostructured Mo-based electrode materials for electrochemical energy storage, Chem. Soc. Rev. 44 (2015) 2376–2404.
[36] Y. Zhang, L. Tao, C. Xie, D. Wang, Y. Zou, R. Chen, Y. Wang, C. Jia, S. Wang, Defect engineering on electrode materials for rechargeable batteries, Adv. Mater. 32 (2020), 1905923.
[37] Y. Zheng, Y. Tang, J.R. Gallagher, J. Gao, J.T. Miller, I.E. Wachs, S.G. Podkolzin, Molybdenum oxide, oxycarbide, and carbide: controlling the dynamic composition, size, and catalytic activity of zeolite-supported nanostructures, J. Phys. Chem. C 123 (2019) 22281–22292.
[38] M. Liu, Y. Yang, X. Luan, X. Dai, X. Zhang, J. Yong, H. Qiao, H. Zhao, W. Song, X. Huang, Interface-synergistically enhanced acidic, neutral, and alkaline hydrogen evolution reaction over Mo_2C/MoO_2 heteronanorods, ACS Sustain. Chem. Eng. 6 (2018) 14356–14364.
[39] Z. Li, C. Zhou, J. Hua, X. Hong, C. Sun, H.-W. Li, X. Xu, L. Mai, Engineering oxygen vacancies in a polysulfide-blocking layer with enhanced catalytic ability, Adv. Mater. 32 (2020), 1907444.
[40] Y. Wu, J. Deng, Y. Zhou, Y. Huang, Y. Li, Molybdenum carbide nanostructures for electrocatalytic polysulfide conversion in lithium-polysulfide batteries, Nanoscale Horiz. 5 (2020) 501–506.
[41] F.Y. Fan, W.C. Carter, Y.-M. Chiang, Mechanism and kinetics of Li_2S precipitation in Lithium-Sulfur batteries, Adv. Mater. 27 (2015) 5203–5209.
[42] Z. Li, Y. Zhou, Y. Wang, Y.-C. Lu, Solvent-mediated Li_2S electrodeposition: a critical manipulator in Lithium-Sulfur batteries, Adv. Energy Mater. 9 (2019), 1802207.
[43] H. Pan, J. Chen, R. Cao, V. Murugesan, N.N. Rajput, K.S. Han, K. Persson, L. Estevez, M.H. Engelhard, J.-G. Zhang, K.T. Mueller, Y. Cui, Y. Shao, J. Liu, Non-

encapsulation approach for high-performance Li-S batteries through controlled nucleation and growth, Nat. Energy 2 (2017) 813–820.
[44] Z. Li, H. Jiang, N.-C. Lai, T. Zhao, Y.-C. Lu, Designing effective solvent-catalyst interface for catalytic sulfur conversion in Lithium–Sulfur batteries, Chem. Mater. 31 (2019) 10186–10196.
[45] J.-L. Yang, D.-Q. Cai, X.-G. Hao, L. Huang, Q. Lin, X.-T. Zeng, S.-X. Zhao, W. Lv, Rich heterointerfaces enabling rapid polysulfides conversion and regulated Li_2S deposition for high-performance Lithium-Sulfur batteries, ACS Nano 15 (2021) 11491–11500.
[46] L. Kong, J.-X. Chen, H.-J. Peng, J.-Q. Huang, W. Zhu, Q. Jin, B.-Q. Li, X.-T. Zhang, Q. Zhang, Current-density dependence of Li_2S/Li_2S_2 growth in Lithium-Sulfur batteries, Energy Environ. Sci. 12 (2019) 2976–2982.
[47] X. Huang, Z. Wang, R. Knibbe, B. Luo, S.A. Ahad, D. Sun, L. Wang, Cyclic voltammetry in Lithium–Sulfur batteries—challenges and opportunities, Energy Technol. 7 (2019), 1801001.
[48] S. Zhou, S. Yang, X. Ding, Y. Lai, H. Nie, Y. Zhang, D. Chan, H. Duan, S. Huang, Z. Yang, Dual-regulation strategy to improve anchoring and conversion of polysulfides in Lithium-Sulfur batteries, ACS Nano 14 (2020) 7538–7551.
[49] S.-H. Chung, C.-H. Chang, A. Manthiram, Progress on the Critical parameters for Lithium-Sulfur batteries to be practically viable, Adv. Funct. Mater. 28 (2018), 1801188.
[50] Y.-J. Yen, S.-H. Chung, Lean-electrolyte lithium-sulfur electrochemical cells with high-loading carbon nanotube/nanofiber-polysulfide cathodes, Chem. Commun. 57 (2021) 2009–2012.
[51] J. Guo, H. Pei, Y. Dou, S. Zhao, G. Shao, J. Liu, Rational designs for Lithium-Sulfur batteries with low electrolyte/sulfur ratio, Adv. Funct. Mater. 31 (2021), 2010499.